Criteria for formation of metallic glasses: The role of atomic size ratio

Hyon-Jee Lee
Materials and Process Simulation Center (MSC), 139-74 and Materials Science Department, 138-78, California Institute of Technology, Pasadena, California 91125

Tahir Cagin
Materials and Process Simulation Center (MSC), 139-74, California Institute of Technology, Pasadena, California 91125

William L. Johnson
Materials Science Department, 138-78, California Institute of Technology, Pasadena, California 91125

William A. Goddard III[a)]
Materials and Process Simulation Center (MSC), 139-74 and Materials Science Department, 138-78, California Institute of Technology, Pasadena, California 91125

(Received 13 September 2002; accepted 12 August 2003)

We consider metallic alloys of Cu*, Cu, and Cu** in which the atoms differ only in their atomic radii and examine how the size ratio affects the local orders in the alloy systems. These studies use molecular dynamics simulations in which the atomic interactions are modeled with a Sutton–Chen many-body potential. Considering rapid cooling of these binary and ternary alloys from the melt, we find three regimes defined by the magnitude of atomic size ratio λ ($\lambda \leqslant 1.0$): with (i) large size ratios of $0.95 < \lambda \leqslant 1.0$, crystallization occurs; (ii) with moderate size ratios of $0.60 \leqslant \lambda \leqslant 0.95$, a glass phase forms; and (iii) with small size ratios of $\lambda < 0.60$, the alloy phase separates into pure phases and crystallize. From analyzing the structures of these binary and ternary alloys, we find that the liquid phase is characterized by local structures in which bonded atoms have local fivefold symmetry, which becomes more prominent as the glass phase forms. For phases that crystallize this local fivefold symmetry disappears as the long-range order of the crystalline phase dominates. The fivefold symmetry in the glass phase is mainly due to the icosahedral cluster formation. Energetically, the formation of icosahedral cluster is favored at the atomic size ratio of $\lambda \sim 0.85$, which is close to the λ at which our analyses shows the maximum in the fivefold symmetry and the number of icosahedral clusters. As λ decreases further, the phase separation is observed. The fivefold symmetry character and the number of icosahedral cluster shows the local minimum at this onset of the phase separation. [DOI: 10.1063/1.1615494]

I. INTRODUCTION

Formation of glasses plays an important role in many technologies, ranging from silica glass, to amorphous semiconductors, to polymers, to amorphous metals. Consequently, the glass transition has been studied in many materials, including polymers (e.g., Polystyrene), metallic alloys (e.g., $Pd_{0.4}Ni_{0.4}P_{0.2}$), ionic systems (e.g., BeF_2), and hydrogen bonded systems (e.g., H_2O, C_2H_5OH).[1] Particularly difficult to form have been glasses of metallic alloys. This is because the highly symmetric building blocks (atoms) and isotropic interactions (metallic bonding) are quite compatible with forming long-range order.

The first discovery of a metallic glass was Au_4Si and, subsequently, many different types of metallic glass alloys have been produced and characterized.[2–4] Some of these metallic glasses exhibit desirable properties for industrial applications, such as low magnetic hysteresis losses (Fe or Co based alloy), high mechanical strength (high yield strength and high elastic strain limit), and high corrosion resistance relative to crystalline alloys with the same composition.[3] However, practical applications have been limited by the high cooling rate (10^5–10^6 K/s) required to form the glass and the difficulty of making bulk (millimeter scale) sized samples.[4]

Recently, new generations of alloys capable of forming a bulk metallic glass (BMG) have been developed by Johnson *et al.*[5] The first family of BMGs (with compositions like $Zr_{41.2}Ti_{13.8}Cu_{12.5}Ni_{10.0}Be_{22.5}$, referred to as Vitreloy 1) form metallic glasses with critical cooling rates of only 1 K/s sufficient to suppress crystallization.[6] Thus Vitreloy 1 has been used to form fully glassy rods with diameters of 5 to 10 cm.[4] This development of BMG forming alloys enables both industrial applications and experimental study of the glass transition and the thermodynamics of supercooled liquid in metallic system.[4]

The discovery of these new generations of BMGs was guided by qualitative reasoning about relative melting and crystallization temperatures of various phases and the role of atomic size ratio (topological disorder) and valence electron

a)Author to whom correspondence should be addressed. Electronic mail: wag@wag.caltech.edu

configuration (chemical disorder) in promoting glass formation while frustrating crystallization.[4] In particular, the atomic size ratio is found to be crucial to frustrate the crystallization.[7,8] Although such qualitative ideas have been useful in making progress, it would be valuable to have a more quantitative understanding of the size ratio effect to promote glass formation and of how this changes as one considers more complex alloys. In addition to that, knowledge of the size ratio effect on the local ordering and phase separation behavior in the glass forming liquid would be interesting both scientifically and for industrial applications, such as controlling of crystallization, fabrication of composites, and production of multiphase *in situ* composites by partial crystallization.

As a first step toward providing this more quantitative understanding and the detailed knowledge of the local ordering and phase separation behavior, we report here systematic studies of the glass forming properties for a series of binary and ternary metallic alloys as a function of the atomic size ratio (λ). These studies use molecular dynamics (MD) with the Sutton–Chen (SC) many-body force field developed to described metallic systems.[9]

We find three regimes of phase behavior upon cooling at a rate of 4×10^{12} K/s, defined by the magnitude of the size ration λ ($\lambda\leqslant1.0$). When λ is close to 1.0, the crystallization occurs upon cooling. In the alloy with $\lambda\leqslant0.95$, glass transition occurs. Examining the details of the changes of structure in the liquid and glass phases, we find that icosahedra dominate the local order in metallic glasses, with $\lambda\sim0.85$ most favoring the formation of icosahedral clusters. Finally, phase separation is observed as λ decreases. The onset of phase separation is $\lambda\sim0.75$ for the binary system and $\lambda\sim0.80$ for the ternary system. Section II outlines the methods and computational details while Sec. III reports the results and discussions.

II. SIMULATION METHODS

A. Force-field and parameters

Many studies of glass formation have used MD and Monte Carlo methods based on systems described with Lennard-Jones pair potentials.[10] Such simulations provide an important theoretical means to study the properties of glasses, including the nature of the glass transition. However, pair potentials have intrinsic limitations for application to metallic systems. For example, homogeneous systems described with pair potentials always satisfy the Cauchy relation $C_{12}=C_{44}$ between elastic constants, whereas metallic systems typically strongly disobey the Cauchy relation.[11] In addition, pair potentials do not capture the effects of electron density on bonding that plays a dominant role in the physical properties of metallic systems. Thus, we believe that it is essential to include many-body interactions in studying the phase behavior of metals and metal alloys. In this work we chose to use the Sutton–Chen (SC) potential,[9] which has a simple power law form and relatively long-range character.

The SC many-body potential has the form

TABLE I. (a) Parameters for the quantum Sutton–Chen (Q-SC) many-body potential for Cu. (b) The lattice constant (α), cohesive energy (E_{coh}), elastic constants (C_{ij}), and bulk modulus (B) calculated using the Q-SC force field parameters in TtN molecular dynamics calculations. Unless otherwise indicated the computed values are for the minimized structures. These values are compared to experimental (Expt.) values at $T=0$ K, unless otherwise indicated.

	ε (meV)	c	m	n	α (Å)
(a)					
Cu	5.7921	84.843	5	10	3.603

	$\alpha(T=0$ K) (A)	$\alpha(T=300$ K) (A)	E_{coh} (eV)	C_{11} (GPa)	C_{12} (GPa)	C_{44} (GPa)	B (GPa)
(b)							
Expt.	3.603	3.615	3.49	176.2	124.9	81.8	142.0
Q-SC	3.603	3.622	3.49	164.5	114.5	71.0	131.2

$$U_{\mathrm{tot}}=\sum_i U_i=\sum_i\left[\tfrac{1}{2}\sum_{j\neq i}\varepsilon_{ij}V(r_{ij})-c_i\varepsilon_{ii}\rho_i^{1/2}\right], \tag{1}$$

$$V(r_{ij})=\left(\frac{\alpha_{ij}}{r_{ij}}\right)^n, \tag{2}$$

$$\rho_i=\sum_{j\neq i}\phi(r_{ij})=\sum_{j\neq i}\left(\frac{\alpha_{ij}}{r_{ij}}\right)^m, \tag{3}$$

where r_{ij} is the distance between atom i and j. $V(r_{ij})$ is a repulsive pair potential between atoms i and j, accounting for the Pauli repulsion between the core electrons. The cohesion associated with atom i is captured in a local energy density ρ_i. ε sets the overall energy scale and c_i is a dimensionless parameter scaling the attractive term. α is a length parameter leading to a dimensionless form for V and ρ.

The force-field parameters for the SC potential were optimized to reproduce experimental properties such as density, cohesive energy, bulk modulus, elastic constants, phonon dispersion, vacancy formation energy, and surface energy. In calculating these properties, we included quantum corrections, leading to the quantum Sutton–Chen, or Q-SC force field.[12] The Q-SC parameter set for Cu used in this study is presented in Table I[12] and has been employed successfully in earlier studies.[8,13]

For alloys we use the following combination rules to describe the interaction between different types of atoms:

$$\varepsilon_{ij}=\sqrt{\varepsilon_{ii}\varepsilon_{jj}}, \tag{4}$$

$$n_{ij}=\tfrac{1}{2}(n_i+n_j), \tag{5}$$

$$m_{ij}=\tfrac{1}{2}(m_i+m_j), \tag{6}$$

$$\alpha_{ij}=\sqrt{\alpha_{ii}\alpha_{jj}}. \tag{7}$$

These combination rules are expected to describe the concentration dependencies of the lattice parameters and elastic constants of alloy systems with good accuracy.[14]

B. Molecular dynamics (MD) studies of alloy systems

To determine the effect of atomic size ratio on the glass transition and crystallization, we changed only the lattice parameter α of the atoms. By changing only the lattice param-

TABLE II. Atom size parameters for the binary and ternary model alloy systems. The parameter λ is defined as the size ratio of Cu* to Cu** in the binary system and Cu* to Cu and Cu to Cu** in the ternary system. These size parameters were chosen to keep constant the geometric mean of the size parameters for Cu* and Cu**, $\alpha_{ij}=\sqrt{\alpha_{ii}\alpha_{jj}}$.

λ	Cu*	Cu**
(a) Binary system		
0.50	2.54 771	5.09 541
0.55	2.67 206	4.85 828
0.60	2.79 087	4.65 145
0.65	2.90 483	4.46 897
0.70	3.01 449	4.30 641
0.75	3.12 029	4.16 039
0.80	3.22 262	4.02 828
0.85	3.32 180	3.90 800
0.90	3.41 811	3.79 790
0.95	3.51 177	3.69 660
1.00	3.60 300	3.60 300

λ	Cu*	Cu	Cu**
(b) Ternary system			
0.50	1.80 150	3.60 300	7.20 600
0.55	1.98 165	3.60 300	6.55 091
0.60	2.16 180	3.60 300	6.00 500
0.65	2.34 195	3.60 300	5.54 308
0.70 711	2.54 771	3.60 300	5.09 541
0.74 162	2.67 206	3.60 300	4.85 828
0.77 460	2.79 087	3.60 300	4.65 145
0.80 623	2.90 483	3.60 300	4.46 897
0.83 666	3.01 449	3.60 300	4.30 641
0.86 603	3.12 029	3.60 300	4.16 039
0.89 443	3.22 262	3.60 300	4.02 828
0.92 195	3.32 180	3.60 300	3.90 800
0.94 868	3.41 811	3.60 300	3.79 790
0.97 468	3.51 177	3.60 300	3.69 660
1.00	3.60 300	3.60 300	3.60 300

eter, we introduced Cu* and Cu**, with the same ε, c, n, and m force field parameters as Cu. The final size parameters for Cu* and Cu** are given in Table II. Note that the λ parameter is the size ratio of *adjacent* sized atoms, i.e., Cu* to Cu** in the binary system and Cu* to Cu or Cu to Cu** in the ternary system.

The binary system is composed of 50% Cu* atoms and 50% Cu** atoms with size ratio $\lambda=\alpha_{Cu*}/\alpha_{Cu**}$ while the ternary system is composed of 1/3Cu*, 1/3Cu, and 1/3Cu** with size ratio $\lambda=\alpha_{Cu*}/\alpha_{Cu}=\alpha_{Cu}/\alpha_{Cu**}$.

The MD simulations were performed using systems with 500 atoms per periodic cell. (For the ternary system we used 167 Cu* and Cu** atoms and 166 Cu atoms.) We used the Parinello–Rahman–Hoover formalism to describe constant temperature constant stress (TtN) conditions.[15] The integration step is chosen to be 1 fs for both high and low temperature simulations.

To generate the liquid phase for each of various alloys, we started with a FCC lattice of Cu** (large atom) and randomly substituted the lattice site with the smaller atoms (Cu* and Cu). This minimized the disturbances caused by size mismatch. Then we equilibrated this alloy for 50 ps with TtN dynamics at $T=300$ K and zero pressure to obtain the starting density. This was followed by a heating cycle in which the system was heated from 300 to 1600 K in increments of 100 K for 25 ps. We found that all systems melted below 1400 K, but we continued to heat to 1600 K to ensure a well-equilibrated melt. The cooling cycle consisted of a similar sequence in which we cooled the sample to 300 K, again in decrements of 100 K for 25 ps.

III. RESULTS AND DISCUSSION

A. The heating and cooling cycles for the $Cu^{*}_{50}Cu^{**}_{50}$ with λ=1.0

Figure 1 shows the results for a single heating-cooling cycle of the binary $Cu^{*}_{50}Cu^{**}_{50}$ system with λ=1.0. This represents the special case in which all atoms are identical to Cu. We melted the system by increasing the temperature in 100 K increments and equilibrating for 25 ps at each temperature, leading to a heating rate of 4×10^{12} K/s. This leads to an initial estimate of the melting temperature by the sharp discontinuity in the volume [Fig. 1(a)] between $T=1200$ K and 1400 K. To obtain a more precise estimate of the melting temperature, we reduced the temperature increment by a factor of 5 to 20 K and decreased the simulation time length by a factor of 5 to 5 ps to maintain a constant heating rate. This leads to the variation of volume versus temperature in Fig. 1(a), which shows a distinct jump in volume (first-order phase transition) corresponding to melting temperature at $T_m=1360\,\mathrm{K}\pm10$ K. This is quite close to the experimentally determined melting temperature $T_m=1358$ K for pure Cu.[16]

The cooling cycle is also shown in Fig. 1(a), where we find crystallization at $T_x=650\,\mathrm{K}\pm50$ K. This is far below the T_m due to the very rapid cooling rate, 4×10^{12} K/s, which leads to considerable supercooling. The final state of the quenched sample at 300 K is a crystal, which is determined by examining the radial distribution function (RDF) at 300 K as shown in Fig. 1(b). For the starting alloy at 300 K the RDF shows the peaks of a FCC structure at σ, $\sqrt{2}\sigma$, $\sqrt{3}\sigma$, 2σ, etc., where σ is the first nearest neighbor distance. In the melt at 1600 K these secondary peaks are gone. However, the quenched structure shows that the FCC pattern is almost recovered. Here the maxima in the third and higher peaks are reduced somewhat but the positions remain the same. This reduction occurs because the cooled crystal at 300 K is not perfect FCC compared to the starting structure. This will be discussed in detail in Sec. III C 2.

A most sensitive measure of the phase transition (to glass or crystal) is provided by extracting the Wendt–Abraham (WA) parameter[17] from the RDF. The Wendt–Abraham parameter is defined by $R^{WA}=g_{min}/g_{max}$ where g_{min} and g_{max} are the magnitudes of the first minimum and first maximum of the radial distribution function (RDF). As shown in Fig. 1(c), the temperature dependence of R^{WA} for a transformation from a liquid to a crystal changes both the magnitude and slope at the transition to the crystal phase, indicating an intrinsic differences in structural properties between a liquid and a crystal. (Below we will see that formation of a glass leads only to a change in slope.)

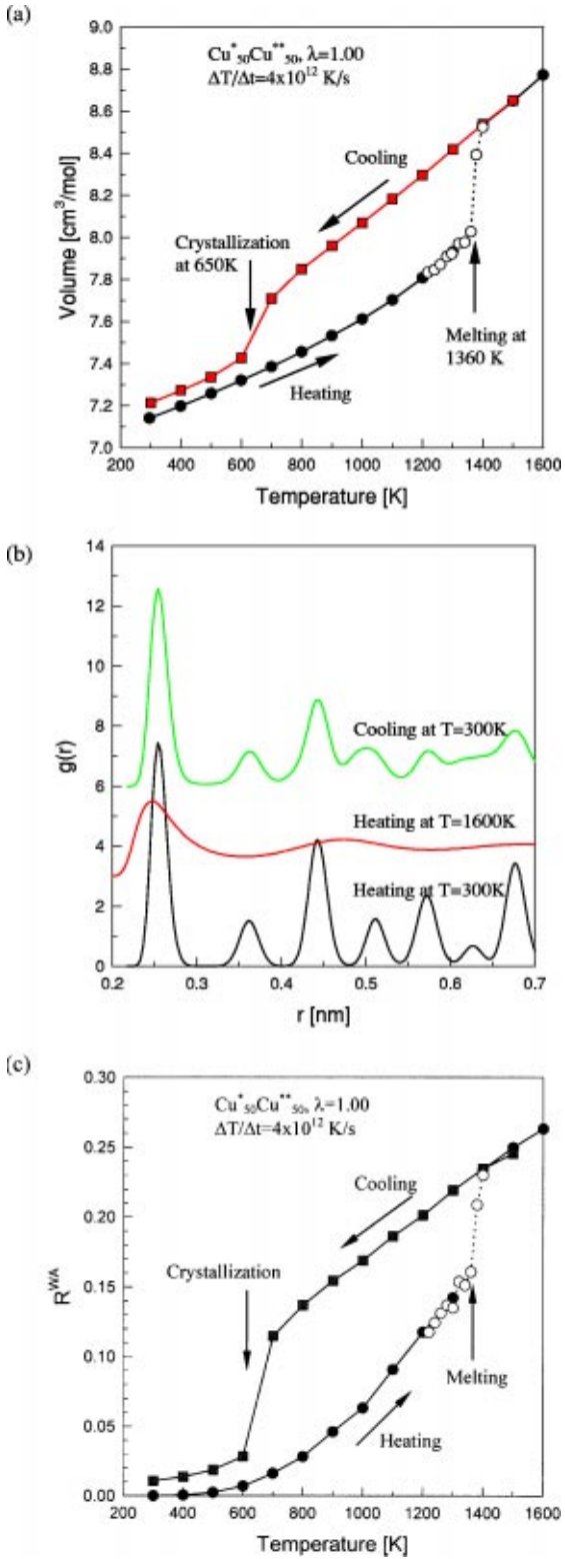

FIG. 1. A heating and cooling cycle of $Cu^{*}_{50}Cu^{**}_{50}$ at $\lambda=1.0$ with a heating/cooling rate of 100 K per 25 ps (4×10^{12} K/s). (a) Volume as a function of temperature. The heating run shows a melting transition at $T=1360$ K ±10 K. Upon cooling, the liquid is supercooled and crystallization occurs at $T=650$ K±50 K. (b) Radial distribution functions (RDF) for three points on the heating and cooling runs; the random FCC crystal starting structure (heating at $T=300$ K); the equilibrated liquid phase (heating at $T=1600$ K); the crystallized systems after quenching (cooling at $T=300$ K). (c) Wendt–Abraham parameter (R^{WA}) as a function of temperature. R^{WA} shows a discontinuity and change in slope at melting and crystallization (first-order transitions), implying the dramatic change in a structural feature.

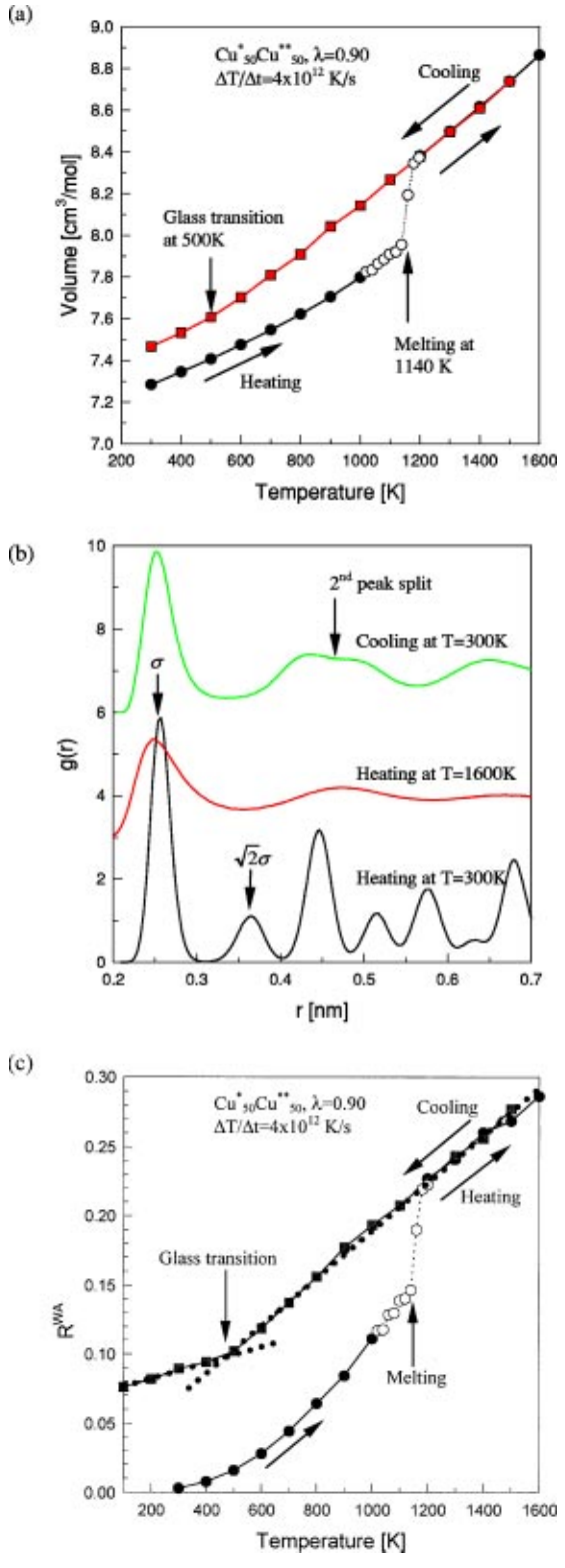

FIG. 2. Heating and cooling cycle of $Cu^{*}_{50}Cu^{**}_{50}$ at $\lambda=0.9$ with a heating/cooling rate of 100 K per 25 ps (4×10^{12} K/s). (a) Volume as a function of temperature. Melting occurs at 1140 K±10 K. Upon cooling, the system transforms into a glass but the volume curve does not provide a clear value for T_g. (b) Radial distribution function (RDF) during heating and cooling runs. Different from the starting structure (a random FCC, heating at $T=300$ K), RDF (cooling at $T=300$ K) shows a bimodal splitting in a second peak, which is a characteristic of amorphous atomic packing. (c) Wendt–Abraham parameter (R^{WA}) as a function of temperature. The R^{WA} changes slope at the glass transition in the cooling run. This leads to $T_g=475$ K ±12 K.

B. The heating and cooling cycles for the $Cu^{*}_{50}Cu^{**}_{50}$ with $\lambda=0.9$

The same heating and cooling procedure was performed for all λ values down to 0.5. Figure 2 shows the results of heating and cooling simulation of the binary system with $\lambda=0.90$. The melting occurs at $T_m=1140\,\mathrm{K}\pm10\,\mathrm{K}$ as shown in Fig. 2(a). Upon cooling, the change of the volume exhibits only subtle changes at the glass transition temperature. We see no dramatic drop in the volume at the glass transition, as observed for the crystallization transition in Fig. 1(a). However, we do see a change in the RDF, as shown in Fig. 2(b). The RDF of cooling simulation at $T=300\,\mathrm{K}$ retains the overall shape of the liquid phase. In contrast with the RDF of heating simulation at $T=300\,\mathrm{K}$, the peak at $\sqrt{2}\sigma$ pair distance is completely absent, which exists only between atoms belong to two adjacent closest packed planes in the FCC or HCP structures. In addition to that, the RDF of cooling simulation at $T=300\,\mathrm{K}$ does show a split in the second peak. This split is indicative of amorphous atomic packing[18] and is observed experimentally in all metallic glasses, but not in liquids.[3]

The temperature dependence of the Wendt–Abraham parameter R^{WA} leads to a clear intersection between two straight lines at $T_g=470\,\mathrm{K}\pm12\,\mathrm{K}$, which indicates the structural arrest by the glass transition. Additional evidence of glass transition can be found in transport properties, such as diffusivity. The temperature dependence of the diffusivity shows a break around the glass transition temperature due to the structural arrest of atoms. Previously, we have measured diffusivity as a function of temperature and confirmed a glass transition.[19]

These studies of melting, crystallization, and the glass transition all as a function of λ provide the material expected to be useful in understanding the thermodynamics of these systems. Consequently, the figures analogous to Figs. 1 and 2 are available in the supplementary material.[20]

C. Structural properties

1. The Honeycutt–Andersen (HA) index

Glasses have no long-range order, making it difficult to analyze the structure. For such systems, we find that a very useful assessment of local structure is provided by Honeycutt and Andersen (HA) analysis,[21] in which the local structure is classified using a sequence of four integers $(ijkl)$, where the following hold:

(1) The first integer (i) is 1 when the atoms in the root pair are bonded, otherwise it is 2.
(2) The second integer (j) is the number of near-neighbor atoms shared in common by the root pair.
(3) The third integer (k) is the number of nearest-neighbor bonds *among* the shared neighbors.
(4) The fourth integer (l) is needed to differentiate between the cases when the first three indices are same but the bond geometries are different.

To define whether two atoms are nearest neighbors, we use the first minimum in the partial radial distribution function (PRDF) for the particular pair of atoms at the temperature (and pressure) being analyzed as the cutoff distance. This accounts for the change in volume resulting from changing temperature (and pressure). Since the atoms have different sizes, we analyze separately all three types of pairs (Cu*–Cu*, Cu**–Cu**, and Cu*–Cu**) in the $Cu^{*}_{50}Cu^{**}_{50}$ binary system, leading to three different cutoff distances for the pair analysis. For the ternary system, this leads to a different cutoff distance for each of the six different kinds of pairs.

TABLE III. Honeycutt–Andersen (HA) pair fractions for several reference systems. Here FCC and HCP denotes bulk systems while ICO_N denotes an icosahedral clusters with N atoms. Thus ICO_13 is a 13-atom icosahedron.

	1311	1321	1421	1422	1551	2331
FCC	0.00	0.00	1.00	0.00	0.00	0.00
HCP	0.00	0.00	0.50	0.50	0.00	0.17
ICO_13	0.00	0.71	0.00	0.00	0.29	0.71
ICO_55	0.26	0.26	0.00	0.38	0.10	0.38
ICO_147	0.26	0.13	0.17	0.39	0.05	0.26
ICO_309	0.23	0.08	0.31	0.35	0.03	0.19

Table III shows the HA analysis for several structures. The pair fractions shown here are normalized so that the sum over all cases for nearest neighbors ($i=1$) add to unity. General observations are as follows:

(i) The FCC structure leads only to 1421 while
(ii) the HCP structure leads to equal amounts of 1421 and 1422.
(iii) A simple icosahedron (ICO_13) has 71% 1321 and 29% 1551 (also 71% 2331) while
(iv) the larger icosahedral structures lead to significant amounts of 1311 and 1422, with decreases in 1321, 1551, and 2331.

Thus, in general, 1421 and 1422 pairs are characteristic of the closest packed crystalline structures (FCC and HCP), while 1321, 1551, and 2331 pairs are characteristics of a simple icosahedral ordering.

2. HA analysis of heating and cooling of the $Cu^{*}_{50}Cu^{**}_{50}$ with $\lambda=1.0$

Figure 3(a) shows the HA pairs as a function of temperature as the binary $Cu^{*}_{50}Cu^{**}_{50}$ system with $\lambda=1.0$ is heated from 300 K to 1600 K. To reduce the statistical error of this analysis, we sampled 200 configurations uniformly separated over the 20 ps and averaged the HA pair analysis results at each temperature. The system starts as a single FCC crystal at $T=300\,\mathrm{K}$, leading only to 1421 pairs. As the temperature increases, the 1421 pair fraction decreases smoothly to ~0.23 at 1340 K, just before melting, drops quickly to 0.03 by 1400 K after melting, and remains constant in the liquid phase.

The 2331 pairs increase rapidly with temperature, to 0.42 just before melting, increasing quickly to 0.65 by 1400 K immediately just after melting. As the temperature increases further, the 2331 pairs decrease slowly, indicating the loss of local order in liquid at high temperature.

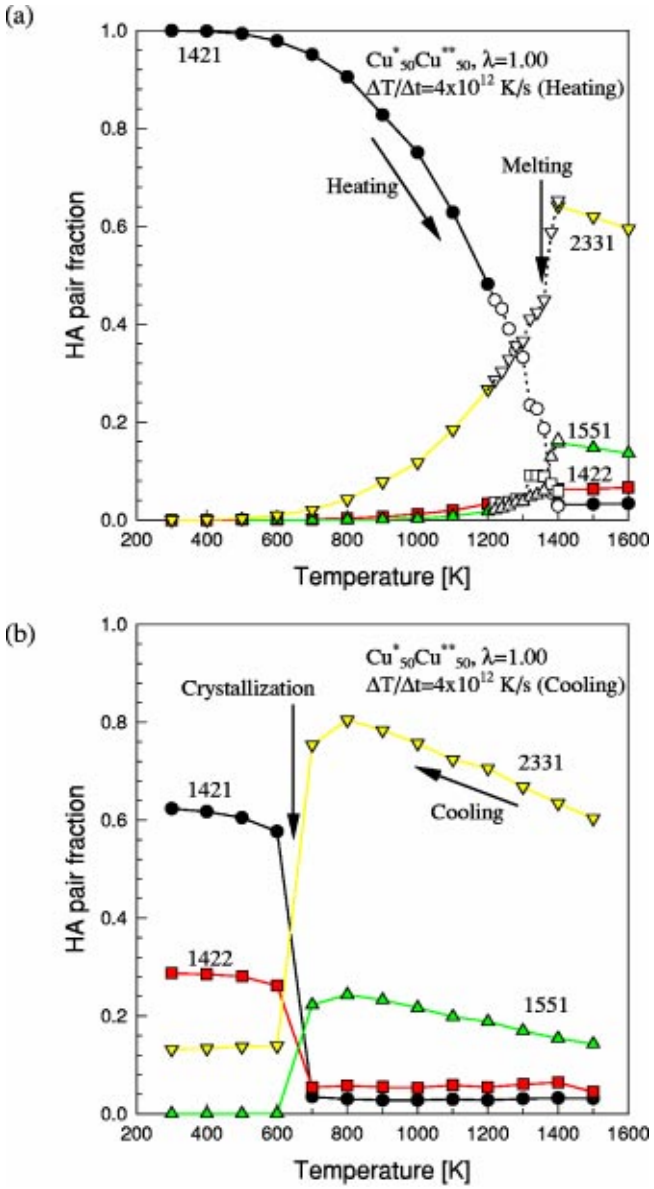

FIG. 3. Honeycutt–Andersen (HA) pair fraction as a function of temperature in $Cu^{*}_{50}Cu^{**}_{50}$ at $\lambda=1.0$ for a heating/cooling rate of 100 K/25 ps (4×10^{12} K/s). (a) **Heating run**. Here we see that the 1421 pairs (characteristic of FCC) decrease gradually as the temperature increases and become almost constant after melting. At the same time the 2331 and 1551 pairs increase as the temperature increases and reach a maximum immediately after melting. (b) **Cooling run**. Here the 1421 and 1422 pairs remain small and constant throughout the supercooled regime and then increase rapidly at crystallization ($T=650$ K). Simultaneously, the 1551 and 2331 pairs increase as the liquid supercools and then decrease abruptly upon crystallization. After crystallization, the 1551 pair fraction becomes zero.

The 1551 pairs follow the behavior of 2331, but less dramatically, reaching to 0.05 just before melting, increasing quickly to 0.16 by 1400 K immediately just after melting. The 1422 characteristic of HCP increases slowly up to T_m and then remains constant at 0.06, nearly twice the value of 1421.

In the cooling simulation [Fig. 3(b)], the 1551 and 2331 pairs increase uniformly as the system supercools, and then decrease abruptly upon crystallization. Here 1551 drops to zero while 2331 drops to a constant value of 0.13.

At the same time the 1421 and 1422 pairs remain almost constant in the liquid and supercooled liquid regime but increase rapidly upon crystallization. The final values after crystallization are 0.62 for 1421 and 0.29 for 1422, indicating that the crystallized sample has mostly FCC and HCP phases. The coexistence of FCC and HCP in a quenched pure Cu system was observed previously in MD simulations.[22] It is mostly this HCP phases that leads to 2331 pairs in the quenched sample after crystallization. The 1.02% increase in volume at $T=300$ K of cooling simulation compared to the heating simulation [Fig. 1(a)] is also due to the formation of a non-FCC phase, such as HCP.

These results show that the 1551 and 2331 pairs are strongly correlated while the 1421 and 1422 pairs are anticorrelated with respect to the 1551 and 2331 pairs. This suggests the existence of two major competing local orders:

(i) close packed FCC/HCP ordering (1421 and 1422 pairs) and
(ii) icosahedral ordering (1551 and 2331 pairs).

3. HA analysis of heating and cooling of the $Cu^{*}_{50}Cu^{**}_{50}$ with $\lambda=0.9$

For the binary system with $\lambda=0.90$, the heating simulation [Fig. 4(a)] shows a more rapid decrease in 1421 pairs than for $\lambda=1.0$, leading to $T_m=1140\,\mathrm{K}\pm10\,\mathrm{K}$, 220 K lower. We attribute this decrease in T_m to the strain energy field generated by the nonequivalent atomic sizes. As for the $\lambda=1.0$ case, the icosahedral 2331 pairs increase rapidly to 0.37 just before melting, jumping to 0.72 by 1200 K (just after melting) and then drop with increasing temperature. Similarly, the icosahedral 1551 jumps from 0.03 just before melting to 0.20 by 1200 K and then drops with increasing temperature. In the melt the 1422 pair remains constant at 0.06, just as for pure Cu.

In the cooling simulation, the 1551 and 2331 pairs increase as the temperature decreases until a maximum at 400 K of 0.97 for 2331 and 0.35 for 1551. Both cases seem to show a bigger increase between 700 and 600 K, but this is not reflected in the WA analysis [Fig. 2(c)].

In contrast with the $\lambda=1.0$ case, the 1421 and 1422 pairs remain almost constant at 0.03 and 0.05, respectively. The preference for 1422 over 1421 in the liquid or glass phase is characteristic of icosahedral clusters where Table III shows that neither occurs for ICO_13, but 1422 is 38% for ICO_55 and 39% for ICO_147, while 1421 is 0% and 17%, respectively.

4. HA analysis of the $Cu^{*}_{50}Cu^{**}_{50}$ at $T=300$ K

Figure 5 shows the HA analysis as a function of λ for samples cooled to 300 K for the binary and ternary systems (again quenched from 1600 K using a 4×10^{12} K/s cooling rate). For $\lambda>0.95$ and higher the system becomes an FCC/HCP crystal upon cooling, showing almost no 1551 pair character. For $\lambda=0.95$ and lower, the system becomes a glass upon cooling, leading large fractions of the 1551 and 2331 pairs. Thus the binary system leads to 2331 over 90% and 1551 over 30% for $\lambda=0.6$ to 0.9. The threshold size ratio for crystallization and glass transition appears to be between

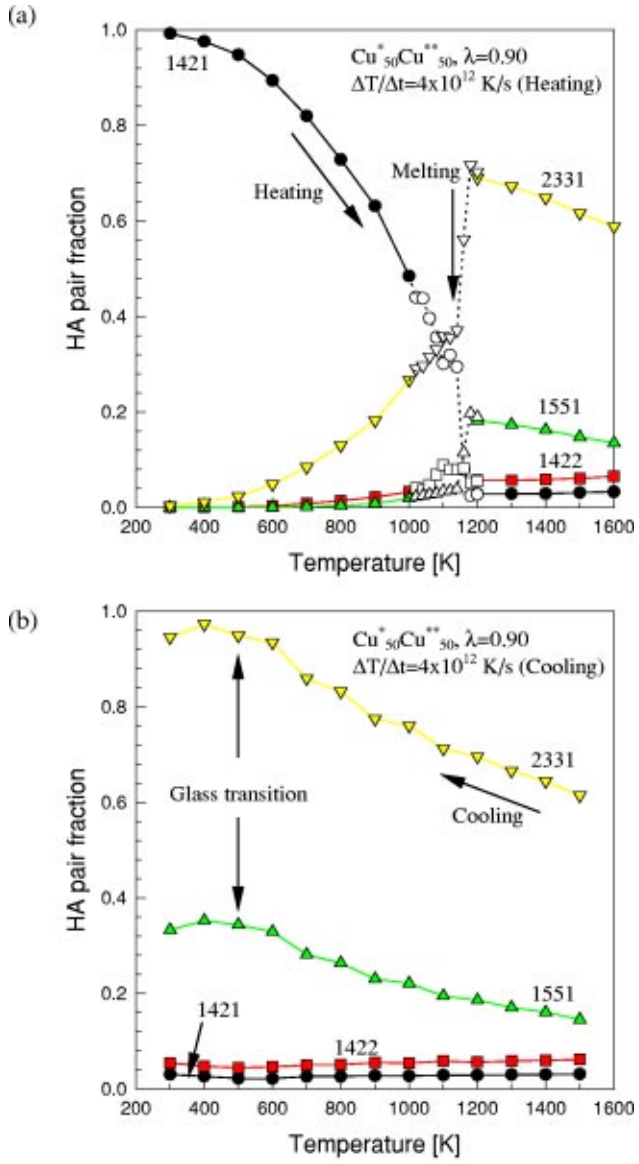

FIG. 4. Honeycutt–Andersen (HA) pair fraction as a function of temperature in $Cu^{*}_{50}Cu^{**}_{50}$ at $\lambda=0.9$ with a heating/cooling rate of 4×10^{12} K/s. (a) **Heating run**. Here the 1421 pairs start to decrease much sooner than for the $\lambda=1.0$ case [Fig. 3(a)], leading to a lower melting temperature. Here the 2331 and 1551 pairs increase slowly as the temperature increases, reaching a maximum immediately after melting. (b) **Cooling run**. Here the 1551 and 2331 pairs increase continuously as the temperature decreases, while the 1421 and 1422 pairs remain relatively constant throughout the run.

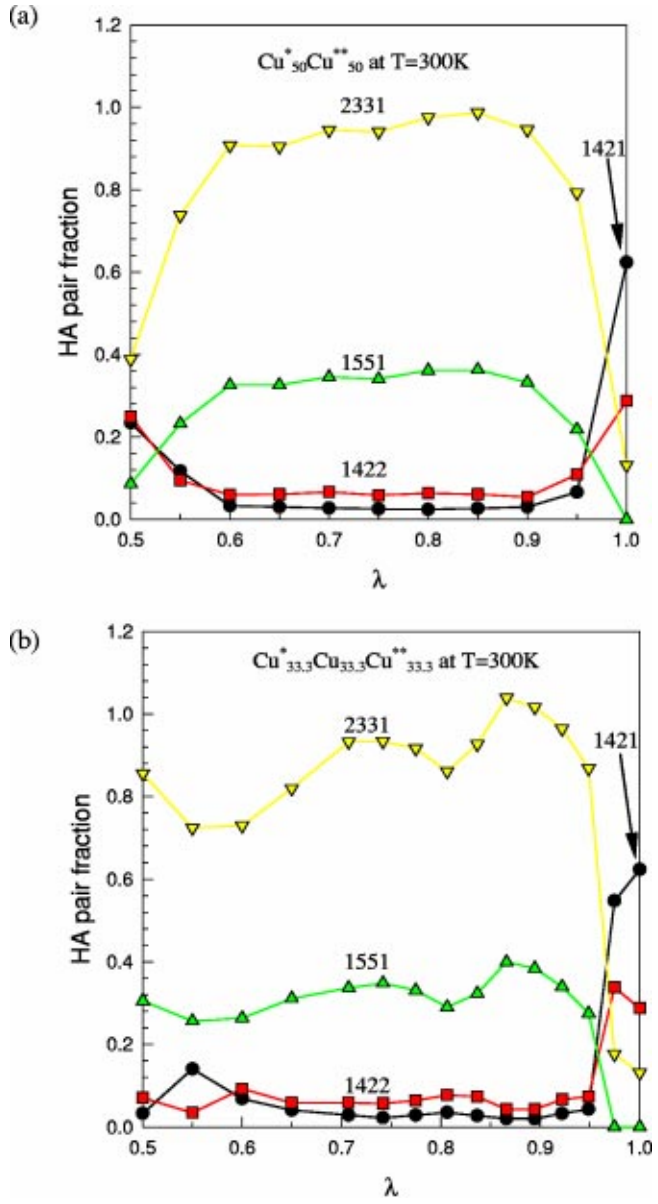

FIG. 5. Honeycutt–Andersen pair fraction as a function of atomic size ratio (λ) at $T=300$ K after the cooling run (cooling rate$=4\times10^{12}$ K/s). (a) **Binary system**. At $\lambda=1.0$, the system has many 1421 and 1422 pairs and almost no 1551 pairs, indicating that it is composed of FCC and HCP phases. As λ decreases, the 1551 and 2331 pairs increase dramatically, showing a maximum at $\lambda\sim0.85$. (b) **Ternary system**. The systems with $\lambda>0.95$ crystallize, leading to large numbers of 1421 and 1422 pairs. Again the 1551 and 2331 pairs increase dramatically as λ decreases, showing a maximum at $\lambda\sim0.87$. However, here the 1551 and 2331 pairs show a local minimum at $\lambda\sim0.8$.

$\lambda=0.95$ and 1.00. In the ternary system, the 1551 and 2331 pairs show a distinct maximum at $\lambda\sim0.85$ while the binary system shows a maximum at 0.85 for 2331 but is rather flat for 1551. For the binary system the 1551 and 2331 pairs decrease abruptly below $\lambda=0.60$ while the 1421 and 1422 pairs increase, implying a partial crystallization. The ternary system shows a more complicated behavior with a local minimum at $\lambda\sim0.8$ in the 1551 and 2331 pair fraction. The phenomena are discussed in more detail in Sec. III D. We should point out that these observations are for quite fast quenching rates of 4×10^{12} K/s. Probably lower quenching rates would have extended the range for forming the crystalline phase to values lower than the $\lambda=0.95$ observed here.

5. Analysis in terms of coordination polyhedra

The coordination polyhedron of an atom is formed by connecting the centers of atoms in the first nearest-neighbor shell with lines. According to this definition, the coordination polyhedra present in the FCC and HCP structures have the shapes of cubo-octahedron (CN_FCC) and twinned cubo-octahedron (CN_HCP), respectively.[23] Both have coordination number (CN) 12, which is the highest possible coordination number for a packing of uniformly sized spheres. In complex structures, a third kind of coordination polyhedron formed by the 12 neighbors, thus the coordination number

TABLE IV. Coordination polyhedra. (a) Geometrical characteristcis of various polyhedra (SC is the surface coordination). (b) The number of Honeycutt-Andersen (HA) pairs in coordination polyhedra.

Type	CN12_FCC	CN12_HCP	CN12	CN14	CN15	CN16
(a)						
Vertices with						
SC=4	12	12	0	0	0	0
SC=5	0	0	12	12	12	12
SC=6	0	0	0	2	3	4
Edges	24	24	30	36	39	42
Faces						
triangular	8	8	20	24	26	28
square	6	6	0	0	0	0
(b)						
1421	12	6	0	0	0	0
1422	0	6	0	0	0	0
1551	0	0	12	12	12	12
1661	0	0	0	2	3	4

12, is present. This is the icosahedron (CN12), which is found in large numbers of the complex crystal structures of transition metal alloys, including the σ phase and the α-manganese structure.[23] However, there is no space-filling structure made up of icosahedron alone due to the fivefold axis of symmetry present in an icosahedron. To have a number of CN12 in structure, Frank and Kasper proposed that higher coordination polyhedra, such as CN14, CN15, or CN16, must be present in complex crystal structures.[24]

Among Frank–Kasper polyhedra, CN12 is often observed experimentally in diffraction patterns of melt-spun metallic glasses.[25] Considering metallic glasses have topologically close packed structures, we think the randomly packed icosahedra with some CN14, CN15, and CN16 can be the characteristic structure of metallic glasses. The HA pair analysis provides a strong evidence of this conjecture by showing large number of the 1551 and 2331 pairs with some 1661 pairs in glasses, which present mostly in Frank–Kasper polyhedra. To clarify the role of local icosahedral ordering and the possible role of other Kasper polyhedra in glasses, we have analyzed the coordination polyhedra for binary and ternary systems described above.

Table IV summarizes the geometrical characteristics of various coordination polyhedra, including their HA pair representations. These characteristics can be used to identify the type of coordination polyhedra present in each sample. For $0.6 \leqslant \lambda \leqslant 0.9$ (glass phases), we find a large number (ranging from 19 to 35 out of total 500) of CN12 polyhedra with one or two CN14, CN15, and CN16 polyhedra but zero or one CN_FCC and CN_HCP. Therefore, we will focus on CN12 in analyzing the coordination polyhedra in glasses.

The bars in Fig. 6(a) show the percentage of CN12 atoms as a function of λ for the binary $Cu^{*}_{50}Cu^{**}_{50}$ system after cooling to $T=300$ K. This is 4% to 7% for $\lambda=0.6$ to 0.9, where essentially all of these icosahedra have the smaller atom Cu* at the center (dark bars). The total number of atoms in these icosahedra (central plus 12 surface atoms) is also shown. This peaks at 50% for $\lambda=0.8$ and is generally above 30% for $\lambda=0.6$ to 0.9. We note that for $\lambda \geqslant 0.75$ the fractions of Cu*, Cu, and Cu** atoms in the icosahedra are almost equal but that for $\lambda<0.75$ there is very distinct fractionalization of the system so that mostly the smaller atoms (Cu*) are associated with icosahedra. This implies heterogeneity in the microstructure and will be explained in connection with the phase separation behavior in Sec. III D.

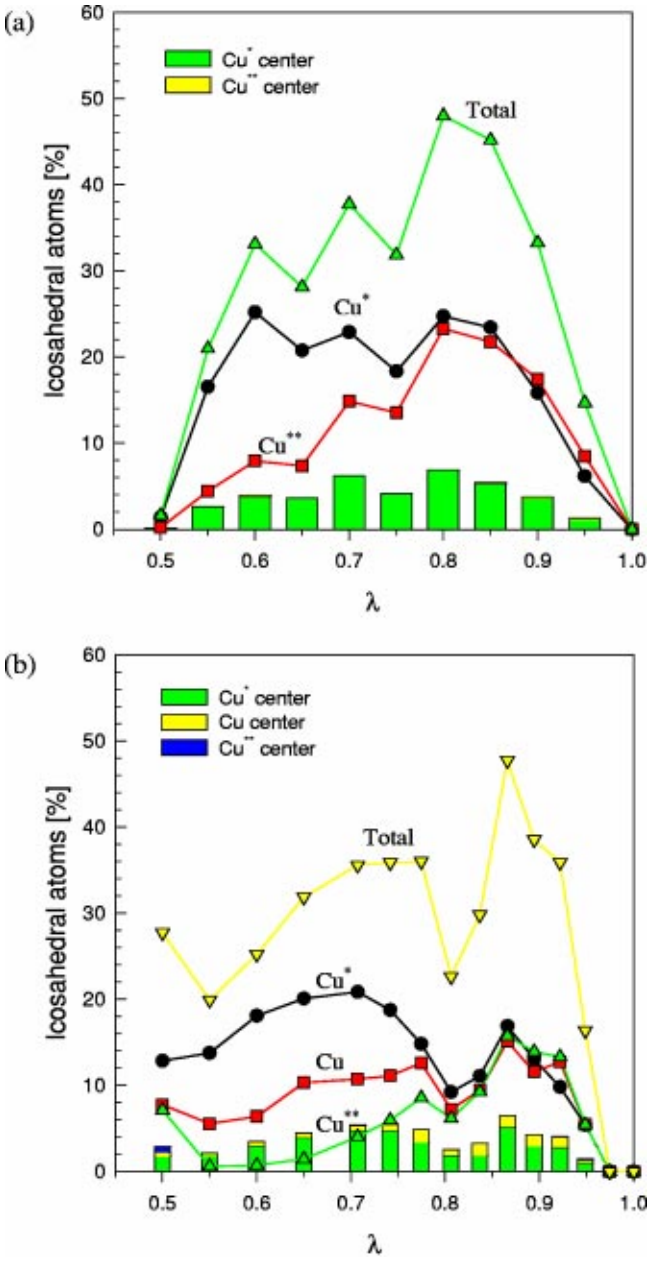

FIG. 6. The symbols and lines show the percentage of atoms contained in icosahedra either at the center (CN12 atoms) or at the surface as a function of λ [for $T=300$ K at the end of the cooling run (cooling rate $=4\times10^{12}$ K/s)]. The stacked bars show a number of CN12 center atoms. The total number of atoms in icosahedra is less than 13 times the number of center atoms of icosahedra because many icosahedra share atoms with other icosahedra. (a) **Binary system**. Interestingly most of the CN/2 center atoms are Cu*, the smaller atom. For $\lambda>0.75$ the concentration of Cu* and Cu** atoms in the icosahedra remains constant. For $\lambda \leqslant 0.75$ the concentrations are clearly disparate, with the icosahedra mostly associated with Cu* (b) **Ternary system**. The number of CN12 center atoms is Cu*>Cu>Cu**. The concentration of Cu*, Cu, and Cu** remains constant above $\lambda \sim 0.8$, while Cu** rapidly disappears from icosahedra for smaller λ.

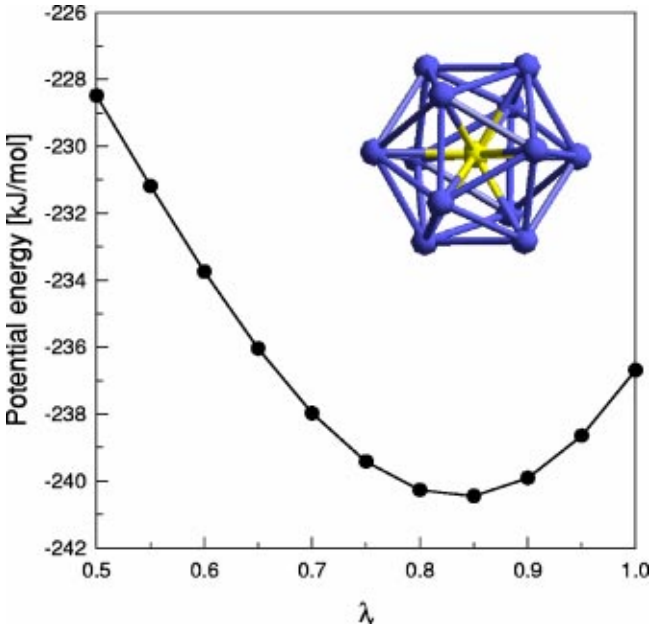

FIG. 7. The minimum potential energy of 13-atom icosahedral cluster as a function of λ. Here, Cu* (light colored ball) is located in the center of the cluster and the 12 Cu** atoms (dark colored ball) are located on the surface. The minimum energy is for λ=0.838 (from a parabolic fit around the minimum).

The results for the ternary system are shown in Fig. 6(b). Here we see a maximum of CN12 atoms at λ=0.87. The majority of CN12 atoms are the smallest ones, Cu*, with the remainder being the middle size, Cu. The total number of atoms in these icosahedra (central plus 12 surface atoms) is also shown. This peaks at 50% for λ=0.87 and is above 37% for λ=0.87 to 0.92. We note that for λ≥0.8 the fractions of Cu*, Cu, and Cu** atoms in the icosahedra are almost equal but that for λ<0.80 there is very distinct fractionalization of the system so that mostly only the smaller atoms are associated with icosahedra with very few of the largest. The bimodal behavior in Fig. 6(b) of icosahedral fraction parallels the behavior in the 1551 and 2331 pairs observed in Fig. 5(b), confirming that these are measuring similar features.

As demonstrated in Fig. 6, the smaller atom is often observed as the center of icosahedral, with binary indicating that the maximum preference for icosahedral occurs for λ=0.80, while ternary shows a maximum preference for λ=0.87. To analyze the origin of this preference, Fig. 7 shows the minimized potential energies of icosahedra as a function of the atomic size ratio λ at $T=0$ K. Here, the small atom (Cu*) is at the center and 12 large atoms (Cu**) are at the surface of the icosahedron. We find that the minimum potential energy for the 13-atom icosahedron is at λ~0.84. Although this study considered only the 13 atoms so that the surface atoms have only six bonds and the number ratio of Cu* to Cu** is 1:12 instead of 1:1, it helps to understand the strong preference of icosahedral structure at λ~0.85 and the preference for Cu* as the icosahedral center atoms (CN12).

6. Analysis of topological connects

Figure 8 illustrates the three-dimensional topology of the icosahedral atoms. The $Cu^{*}_{50}Cu^{**}_{50}$ system with λ=0.85 is shown in Figs. 8(a)–8(d). The center of CN12 (icosahedra) is shown as dark balls, which are connected with solid lines when they share atoms in their first coordination shell. The atoms in the CN12 coordination shell are shown as light balls.

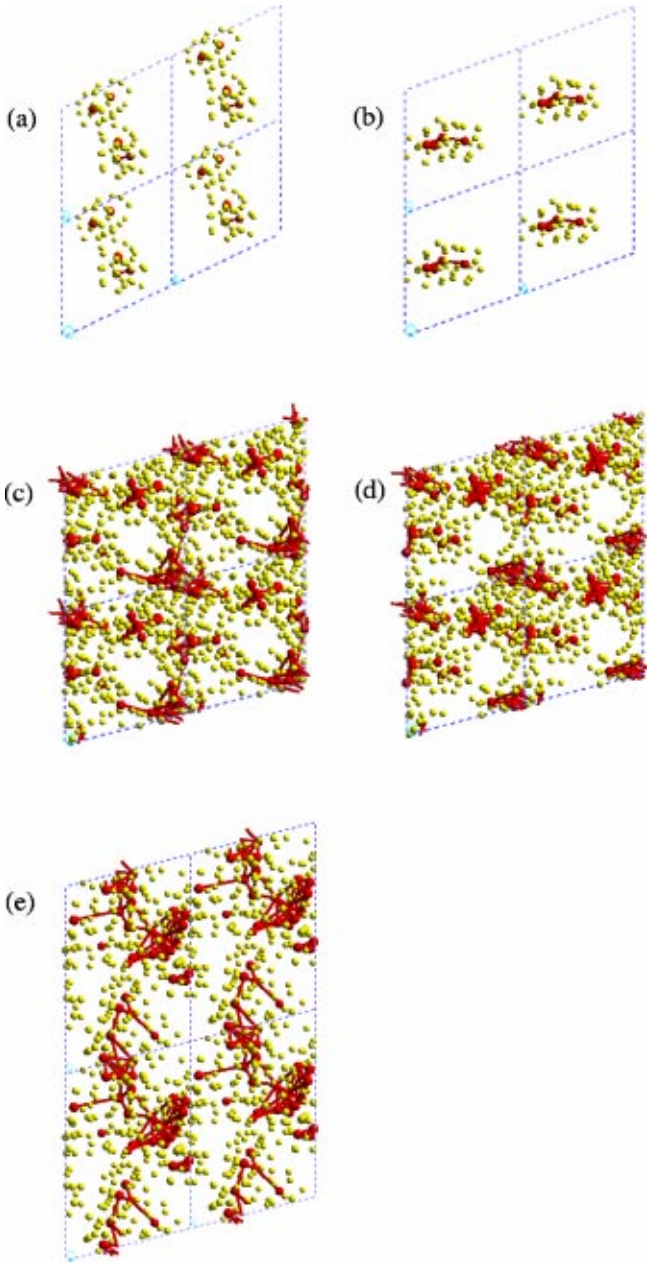

FIG. 8. The topology of icosahedral ordering. Here we show the projection of four unit cells on the *xy* plane. The centers of icosahedra are shown as dark balls which are connected with a solid line if they interpenetrate (center atoms bonded, thus sharing five common neighbors, i.e., 1551), share a face (center atoms share three common neighbor atoms, i.e., 1331), share a line (center atoms share two common neighbor atoms), or share a vertex (center atoms share one common neighbor atom): (a) $Cu^{*}_{50}Cu^{**}_{50}$ system with λ=0.85, at $T=800$ K, at time=0.1 ps; (b) $Cu^{*}_{50}Cu^{**}_{50}$ system with λ=0.85, at $T=800$ K, at time=20.0 ps; (c) $Cu^{*}_{50}Cu^{**}_{50}$ system with λ=0.85, at $T=300$ K, at time=0.1 ps; (d) $Cu^{*}_{50}Cu^{**}_{50}$ system with λ=0.85, at $T=300$ K, at time=20.0 ps; and (e) $Cu^{*}_{33.3}Cu_{33.3}Cu^{**}_{33.3}$ system with λ=0.86603, at $T=300$ K, at time=20 ps.

Figures 8(a) and 8(b) show snapshots at $T=800$ K (above the glass transition) separated by 19.9 ps. Here we see

somewhat similar structural patterns but with different atoms. This suggests that above the glass temperature there are fewer icosahedron atoms (average over 20 ps simulation gives five icosahedron center atoms out of 500 atoms) and that the icosahedral domains are dynamic and fluctuating.

Figures 8(c) and 8(d) show the same system at $T=300\,\mathrm{K}$, well below the glass transition temperatures again separated by 19.9 ps. There are more icosahedron atoms and the icosahedral domains persist throughout the simulation at $T=300\,\mathrm{K}$.

These results combined with the temperature dependence of the icosahedral pairs (1551 and 2331) in Fig. 4(b) suggest the following pictures. For temperatures above the T_g, decreasing temperature leads to increased numbers of CN12 centers, which at higher temperatures are ephemeral and not highly connected [as in Figs. 8(a) and 8(b)]. As these icosahedral domains grow with decreasing temperature, they interconnect which slows the dynamic variations. At some point the interlocking of these domains is sufficient (perhaps when the interconnections become infinite, i.e., when they percolate) that the domain structure remains constant. This may correspond to the glass transition temperature. If so, this may be very similar to the formation of glassy or amorphous phases in polymers.

The $Cu^{*}_{33.3}Cu_{33.3}Cu^{**}_{33.3}$ system with $\lambda=0.87$ is shown in Fig. 8(e) for 300 K. Here we see interlocking icosahedral domains much as in Figs. 8(c) and 8(d) for the binary case, suggesting a similar picture.

D. Phase separation

1. Binary system

Figure 9(a) shows the quenched structure at 300 K for the binary $Cu^{*}_{50}Cu^{**}_{50}$ system with $\lambda=0.50$. Here it is quite clear that there are two separate phases (Cu* phase and Cu** phase) with a well-defined phase boundary.

In Fig. 9(a) the Cu* phase appears to be disordered while the Cu** phase appears to be ordered. This is made more clear in Fig. 9(b) showing the Cu*–Cu* partial RDF (PRDF) in the liquid phase (1600 K) and upon cooling to 300 K. This shows that the Cu* has become a glass [second peak at 0.33 nm is split just as in Fig. 2(b)], but there is a small amount of close packed crystalline character [the small bump at $r=\sqrt{2}\sigma$, as in Fig. 1(b)]. Also, the HA analysis on the Cu* phase gives pair fraction values of 0.13 for 1421 pairs, 0.13 for 1422 pairs, 0.09 for 1551 pairs, and 0.48 for 2331 pairs, indicating the coexistence of crystalline and glass structures.

On the other hand, the PRDF of the Cu** phase in Fig. 9(c) shows a clear crystalline character. In addition the HA analysis on this Cu** phase gives pair fraction values of 0.38 for 1421 pairs, 0.41 for 1422 pairs, 0.02 for 1551 pairs, and 0.10 for 2331 pairs. Again, this indicates crystalline character. Given that the Cu** have crystallized, we speculate that the lack of crystallizing of the Cu* here may be because the atomic size ratio effect on the interface per unit volume is bigger in Cu* phase combined with the rapid quenching.

To further quantify this phase separation behavior, Fig. 10 shows the pair fraction (defined as the number of a specific pair type present in the sample normalized by the total number of pairs in the system) after quenching at $T=300\,\mathrm{K}$ as a function of λ. For a binary system with $\lambda=1.0$, a random alloy should give 0.25 for like pairs (Cu*–Cu* and Cu**–Cu**) and 0.50 for unlike pairs (Cu*–Cu**), which is very close to the observed values in Fig. 10. As λ de-

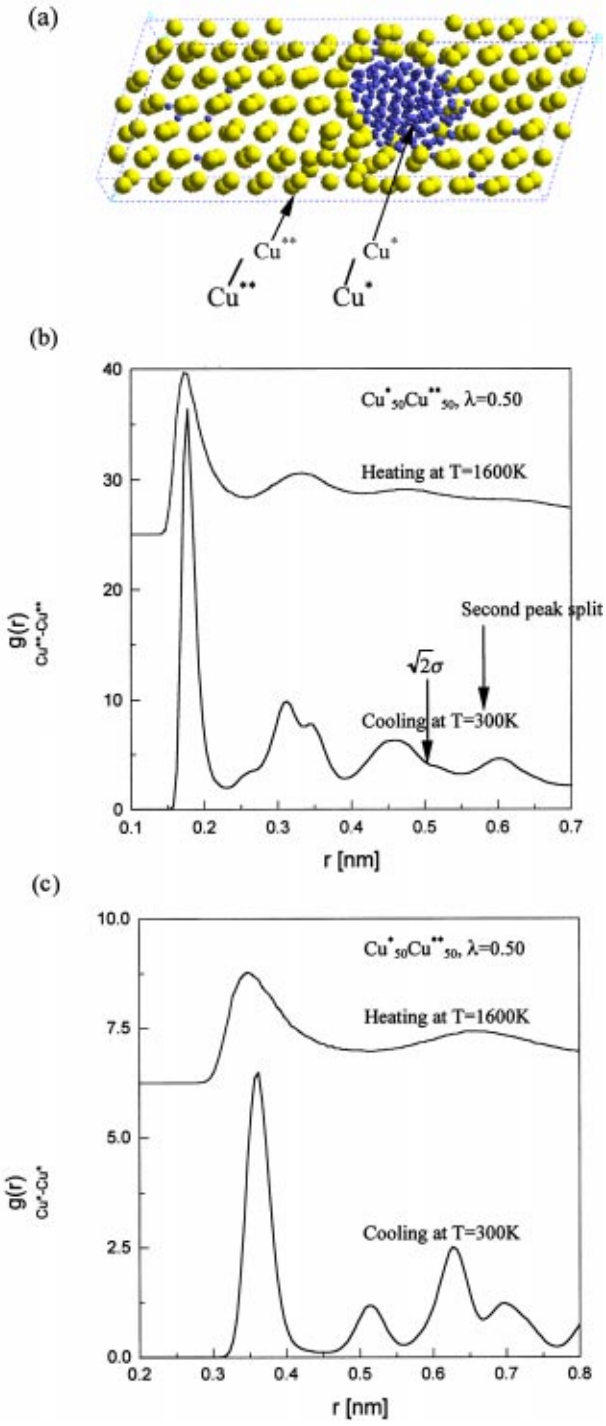

FIG. 9. Binary alloy with $\lambda=0.50$ at 300 K after cooling from the liquid state ($T=1600\,\mathrm{K}$). (a) A snapshot, one unit cell. Dark colored small balls are Cu* and light colored big balls are Cu**. Cu* and Cu** are phase separated with Cu** showing crystalline order. (b) Partial radial distribution function (PRDF) of Cu*, showing a predominance of amorphous packing (second peak split) but some FCC character. (c) PRDF of Cu** showing FCC order.

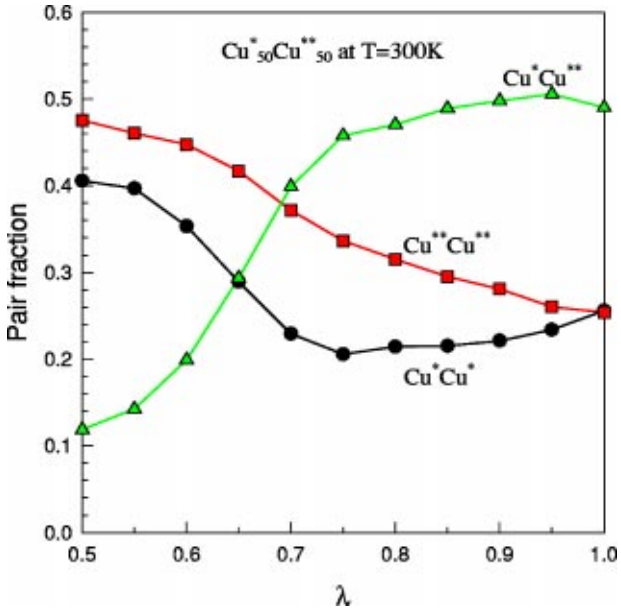

FIG. 10. The pair fraction in the binary system as a function of λ. The fraction of unlike pairs (Cu*–Cu**) is nearly constant above λ~0.75, but decreases rapidly below 0.75, indicating the onset of a phase separation.

creases, the fraction of unlike pairs decreases due to the phase separation between different atomic species. The decrease of unlike pair fraction becomes abrupt at λ~0.75, indicating the existence of a threshold λ for phase separation.

Finally, we found that the phase separation behavior is closely related to the number of icosahedral atoms present in the glass phases. At the onset of phase separation (λ~0.75), the icosahedral character shows a local minimum [Fig. 6(a)] and the concentrations of each atom in icosahedra start to change noticeably as λ decreases further. The smaller atoms (Cu*) are more involved in forming icosahedra at this λ range (λ<0.75). This suggests the higher glass forming chances of Cu* over Cu** in the alloy system at small λ, which agrees with our observation in Fig. 9.

2. Ternary system

As shown in Fig. 11(a), ternary systems show an even more pronounced phase separation behavior among Cu*, Cu, and Cu**. Here we see a strong phase separation between the smallest (Cu*) and the largest (Cu**), with the intermediate size (Cu) forming an interfacial layer between the two phases. This is because the size ratio of Cu* to Cu** is 0.30

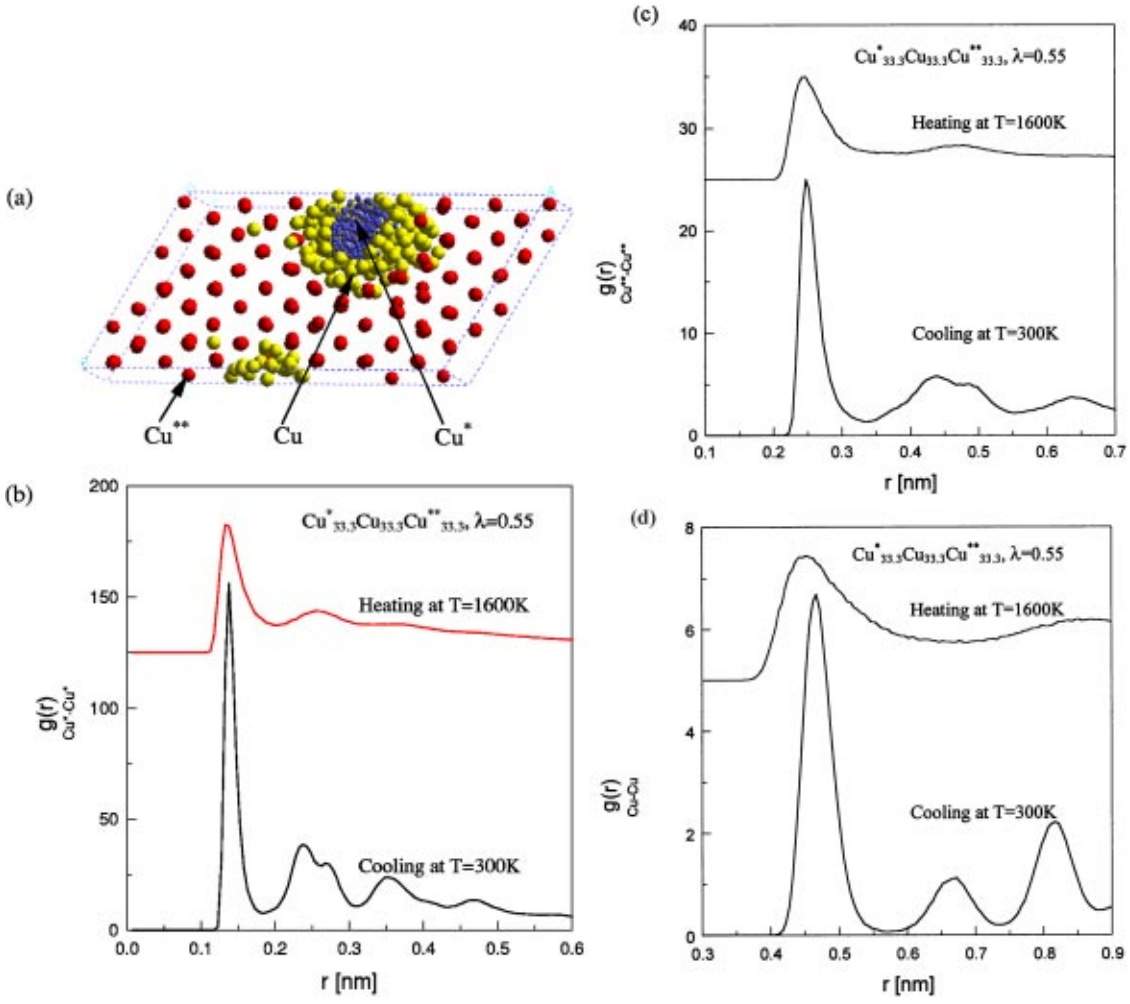

FIG. 11. Ternary alloy with λ=0.55 at 300 K after cooling from the liquid state ($T=1600$ K). (a) A snapshot, showing one unit cell. Dark colored small balls are Cu*, light colored big balls are Cu, and dark colored big balls are Cu**. Cu*, Cu, and Cu** are phase separated with Cu** showing crystalline order. (b) PRDF of Cu* shows an amorphous packing at $T=300$ K. (c) PRDF of Cu shows an amorphous packing at $T=300$ K. (d) PRDF of Cu** shows a FCC order at $T=300$ K.

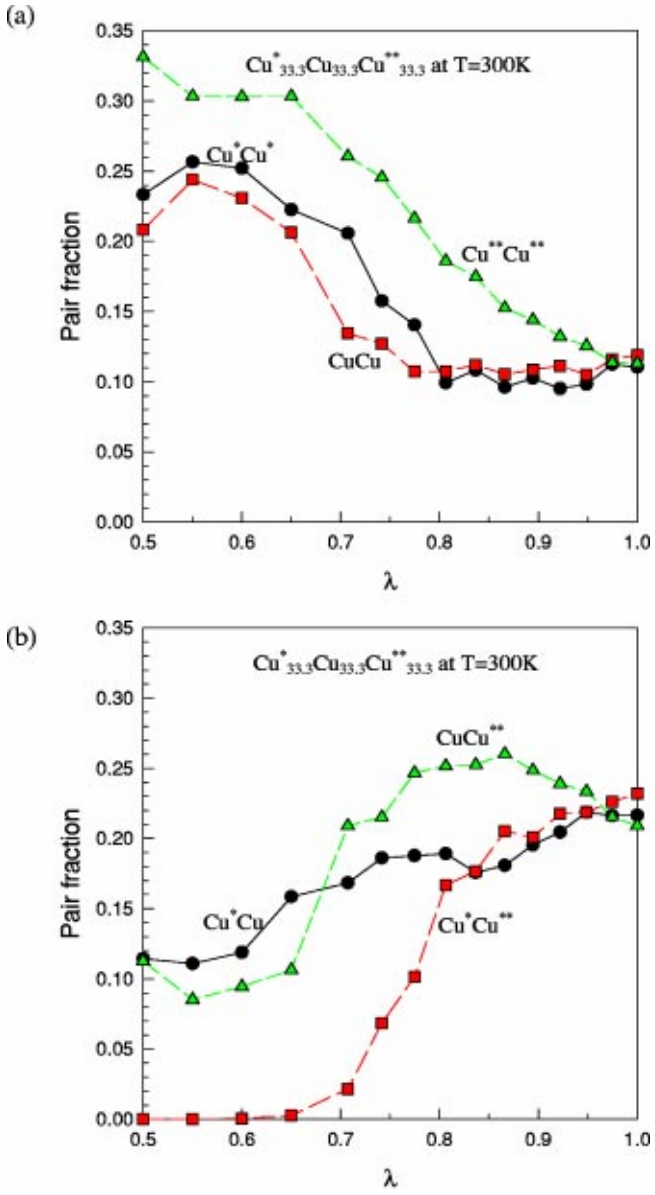

FIG. 12. The pair fraction in the ternary system as a function of λ. (a) Like pairs (Cu*–Cu*, Cu–Cu, and Cu**–Cu**). (b) Unlike pairs (Cu*–Cu, Cu*–Cu**, and Cu–Cu**). The Cu**–Cu** fraction increases uniformly as λ decreases from 1 to 0.65 while the other like interactions remain constant above λ∼0.80. Below this value (λ∼0.80) the Cu*–Cu** pair fraction decreases abruptly, indicating the onset of phase separation.

when the Cu* to Cu and Cu to Cu** ratios are 0.55 [Table II(b)]. Therefore, it is favorable to make Cu*/Cu and Cu/Cu** interfaces rather than a Cu*/Cu** interface to accommodate the size ratio induced phase separation. The separated Cu*, Cu, and Cu** phase become either glass or crystal depending on the magnitude of the size ratio and the phase separation. The Cu**–Cu** PRDF in Fig. 11(d) shows that the Cu** phase in Fig. 11(a) is crystalline. However, the second peak splits of PRDF in Fig. 11(b) for Cu*–Cu* and in Fig. 11(c) for Cu–Cu indicate that these phases are disordered (glasses).

Figure 12 shows the pair fraction for the ternary systems after quenching to $T=300$ K. The ternary system also demonstrates phase separation among Cu*, Cu, and Cu** as λ decreases [like pairs in Fig. 12(a) and unlike pairs in Fig. 12(b)]. In particular, the Cu*–Cu** pair fraction decreases rapidly at λ∼0.8 and becomes almost zero at λ<0.7. This implies that Cu* and Cu** have nearly no contact at λ<0.7, which is made possible by having the Cu layer between the Cu* phase and the Cu** phase [Fig. 11(a)].

At the onset of phase separation (λ∼0.8), ternary systems also show a local minimum in the icosahedral character [Figs. 5(b) and 6(b)]. As λ decreases further, the concentration of each atom in icosahedra becomes Cu*>Cu>Cu** as shown in Fig. 6(b). This also corresponds to the higher glass-forming chances of each atom in the order of Cu*>Cu>Cu**, which agrees with our observation in Fig. 11.

E. Phase diagram

The phase diagrams give important information in controlling crystallization and phase separations. Several methods have been developed and used to calculate phase diagrams using MD or MC simulations with hard sphere model or LJ potential.[26,27] In particular, Hitchcock and Hall's paper[27] describes how the size ratio and the potential well depth ratio change the phase diagram in the model LJ mixtures. Although they used LJ potential, we predict that the qualitative feature of phase diagrams of model LJ systems would be similar to that of the model many-body potential systems. Some general properties obtained from this study, such as the melting point change as a function of size ratio, show a good agreement with the description of the phase diagram in the model LJ systems. The detailed calculation of phase diagrams using many-body potential is currently on the way and will be available in a separate paper.

In addition to the size ratio, it would be interesting to study the potential well depth ratio (ε) effect on the structural properties of alloy systems. Previously, we observed phase separation at λ=0.5 and potential well-depth ratio=1.0, but we saw the NaCl structure formation at λ=0.5 and potential well-depth ratio=0.125.[28] This suggests that structural properties such as phase separation behavior and intermetallic compound formation are a function of λ and the potential well-depth ratio. Therefore, it would be helpful to construct phase diagrams in a broad range of λ and potential well-depth ratio range of constituting elements using a realistic potential to relate these to the structural properties.

IV. CONCLUSION

To investigate the atomic size ratio effect on the local orders in metallic alloys, we carried out molecular dynamics simulations using the Q-SC many-body force field as a function of the atomic size ratio (λ≤1.0). Upon melting, the alloy system shows an abrupt increase in the local fivefold symmetry of bonding, which does not exist in the initial crystalline state. As the system is cooled from its liquid state, this fivefold symmetry keeps increasing until the system reaches the phase transition point. We find three regimes of phase transition behavior, defined by the magnitude of the atomic size ratio λ:

(i) When $0.95<\lambda\leqslant 1.0$, crystallization occurs easily upon cooling.
(ii) As λ decreases, we find glass formation.
(iii) As λ decreases further, we observe phase separation rather than glass formation.

The local fivefold symmetry of bonding disappears abruptly upon crystallization, however, it stays rather constant upon glass transition due to the structural arrest.

Using Honeycutt–Anderson pair index analysis and coordination polyhedra analysis, we find that the local fivefold symmetry of bonding is largely due to the icosahedra formation. In particular, the icosahedra dominate the local order in metallic glasses, with $\lambda\sim 0.85$ most favoring the formation of icosahedral clusters. This is because the $\lambda\sim 0.85$ is energetically most favored in forming icosahedral clusters. Also, we find that mostly the smaller atoms are situated as the center of icosahedra in metallic glasses.

As λ decreases further, the phase separation is observed. Generally, the phase separation promotes crystallization, thus lowering the glass forming ability. The onset of the phase separation is determined as $\lambda\sim 0.75$ (binary system) and $\lambda\sim 0.80$ (ternary system). The fivefold symmetry character and the number of icosahedral clusters show the local minimum at this onset of the phase separation.

ACKNOWLEDGMENTS

We thank Dr. Alejandro Strachan for many helpful discussions. This work was supported in part by the MRSEC Program of the National Science Foundation under Award Nos. DMR-0080065 and ARO-DARPA-SAM project. The facilities of the MSC used for these studies were funded partly by NSF MRI, ARO/DURIP, and IBM-SUR. In addition, support for the MSC is also provided by grants from DOE-ASCI, ARO/MURI, ChevronTexaco, NIH, ONR, Seiko-Epson, Avery-Dennison, Kellogg's, General Motors, Beckman Institute, Asahi Kasei, Toray, and Nippon Steel.

[1] R. Zallen, *The Physics of Amorphous Solids* (Wiley-Interscience, New York, 1998).
[2] W. Klement, R. H. Willens, and P. Duwez, Nature (London) **187**, 869 (1960).
[3] *Metallic Glasses*, edited by P. Duwez (American Society for Metals, Metals Park, OH, 1978).
[4] W. L. Johnson, in *Maternal Research Society Symposium Proceedings*, edited by W. L. Johnson, A. Inoue, and C. T. Liu (Materials Research Society, Boston, MA, 1998), Vol. 554, p. 311.
[5] A. Peker and W. L. Johnson, Appl. Phys. Lett. **63**, 2342 (1993).
[6] Y. J. Kim, R. Busch, W. L. Johnson, A. J. Rulison, and W. K. Rhim, Appl. Phys. Lett. **65**, 2136 (1994).
[7] T. Egami and Y. Waseda, J. Non-Cryst. Solids **64**, 113 (1984).
[8] Y. Qi, T. Cagin, Y. Kimura, and W. A. Goddard, Phys. Rev. B **59**, 3527 (1999).
[9] A. P. Sutton and J. Chen, Philos. Mag. Lett. **61**, 139 (1990).
[10] L. V. Woodcock, C. A. Angell, and P. Cheeseman, J. Chem. Phys. **65**, 1565 (1976); F. F. Abraham, *ibid.* **72**, 359 (1980); J. R. Fox and H. C. Andersen, J. Phys. Chem. **88**, 4019 (1984); H. Jonsson and H. C. Andersen, Phys. Rev. Lett. **60**, 2295 (1988); G. Wahnstrom, Phys. Rev. A **44**, 3752 (1991); M. Li and W. L. Johnson, Phys. Rev. Lett. **70**, 1120 (1993); W. Kob, J. Phys.: Condens. Matter **11**, R85 (1999).
[11] J. F. Thomas, Scr. Metall. **5**, 787 (1971).
[12] Y. Kimura, T. Cagin, Y. Qi, and W. A. Goddard III (unpublished).
[13] Y. Qi, T. Cagin, Y. Kimura, and W. A. Goddard, J. Comput.-Aided Mater. Des. **8**, 233 (2002); H. Ikeda, Y. Qi, T. Cagin, K. Samwer, W. L. Johnson, and W. A. Goddard, Phys. Rev. Lett. **82**, 2900 (1999); T. Cagin, G. Dereli, M. Uludogan, and M. Tomak, Phys. Rev. B **59**, 3468 (1999).
[14] H. Rafiitabar and A. P. Sutton, Philos. Mag. Lett. **63**, 217 (1991).
[15] M. Parrinello and A. Rahman, Phys. Rev. Lett. **45**, 1196 (1980); W. G. Hoover, Phys. Rev. A **31**, 1695 (1985); J. R. Ray and A. Rahman, J. Chem. Phys. **82**, 4243 (1985).
[16] C. Kittel, *Introduction to Solid State Physics*, 7th ed. (Wiley, New York, 1996).
[17] H. R. Wendt and F. F. Abraham, Phys. Rev. Lett. **41**, 1244 (1978).
[18] J. L. Finney, Nature (London) **266**, 309 (1977).
[19] H.-J. Lee, Y. Qi, A. Strachan, T. Cagin, W. A. Goddard III, and W. L. Johnson, in *Material Research Society Symposium Proceedings*, edited by A. R. Y. A. Inoue, W. L. Johnson, and R. H. Dauskardt (Materials Research Society, Boston, MA, 2001), Vol. 644, p. L2.3.1.
[20] H.-J. Lee, Ph.D. thesis, California Institute of Technology, 2003.
[21] J. D. Honeycutt and H. C. Andersen, J. Phys. Chem. **91**, 4950 (1987).
[22] C. S. Liu, J. C. Xia, Z. G. Zhu, and D. Y. Sun, J. Chem. Phys. **114**, 7506 (2001).
[23] W. Hume-Rothery, R. E. Smallman, and C. W. Haworth, *The Structure of Metals and Alloys* (Institute of Metals, London, 1969).
[24] F. C. Frank and J. S. Kasper, Acta Crystallogr. **11**, 184 (1958).
[25] J. Saida, M. Matsushita, C. Li, and A. Inoue, Appl. Phys. Lett. **76**, 3558 (2000).
[26] B. B. Laird and A. D. J. Haymet, Mol. Phys. **75**, 71 (1992); M. D. Eldridge, P. A. Madden, and D. Frenkel, Nature (London) **365**, 35 (1993); X. Cottin and P. A. Monson, J. Chem. Phys. **102**, 3354 (1995); D. A. Kofke, Mol. Phys. **78**, 1331 (1993).
[27] M. R. Hitchcock and C. K. Hall, J. Chem. Phys. **110**, 11433 (1999).
[28] H.-J. Lee, T. Cagin, W. A. Goddard III, and W. L. Johnson, J. Metastable Nanocryst. Mater. **15-16**, 181 (2003).